## Highly spin-polarized multi-GeV electron beams generated by single-species plasma photocathodes

Zan Nie , <sup>1,\*</sup> Fei Li , <sup>1,†</sup> Felipe Morales, <sup>2</sup> Serguei Patchkovskii, <sup>2</sup> Olga Smirnova, <sup>2</sup> Weiming An, <sup>3</sup> Chaojie Zhang, <sup>1</sup> Yipeng Wu, <sup>1</sup> Noa Nambu, <sup>1</sup> Daniel Matteo, <sup>1</sup> Kenneth A. Marsh, <sup>1</sup> Frank Tsung, <sup>4</sup> Warren B. Mori, <sup>1,4</sup> and Chan Joshi <sup>1,‡</sup> 

<sup>1</sup> Department of Electrical and Computer Engineering, University of California, Los Angeles, California 90095, USA

<sup>2</sup> Max Born Institute, Max-Born-Strasse 2A, D-12489 Berlin, Germany

<sup>3</sup> Department of Astronomy, Beijing Normal University, Beijing 100875, China

<sup>4</sup> Department of Physics and Astronomy, University of California, Los Angeles, California 90095, USA

(Received 18 January 2022; accepted 2 May 2022; published 8 July 2022)

High-gradient and high-efficiency acceleration in plasma-based accelerators has been demonstrated, showing its potential as the building block for a future collider operating at the energy frontier of particle physics. However, generating and accelerating the required spin-polarized beams in such a collider using plasma-based accelerators have been a long-standing challenge. Here we show that the passage of a highly relativistic, high-current electron beam through a single-species (ytterbium) vapor excites a nonlinear plasma wake by primarily ionizing the two outer 6s electrons. Further photoionization of the resultant  $Yb^{2+}$  ions by a circularly polarized laser injects the  $4f^{14}$  electrons into this wake, generating a highly spin-polarized beam. Combining time-dependent Schrödinger equation simulations with particle-in-cell simulations, we show that a subfemtosecond, high-current (4 kA) electron beam with up to 56% net spin polarization can be generated and accelerated to 15 GeV in just 41 cm. This relatively simple scheme solves the perplexing problem of producing spin-polarized relativistic electrons in plasma-based accelerators.

DOI: 10.1103/PhysRevResearch.4.033015

#### I. INTRODUCTION

High-brightness relativistic spin-polarized beams play indispensable roles in high-energy physics, such as in highenergy lepton colliders [1] and parity violation experiments [2,3]. However, conventional radio-frequency-based accelerators that can reach the necessary energies at the energy frontier of collider-based particle physics will become gargantuan and prohibitively expensive. By demonstrating an orders of magnitude higher accelerating gradient and a high-energy extraction efficiency, a plasma-based accelerator (PBA) offers a paradigm-changing alternative that promises to shrink the size and cost of future high-energy colliders [4]. However, a practical scheme for generating and accelerating spin-polarized leptons in PBAs is still lacking. Conventional methods of generating spin-polarized electrons include self-polarization via the Sokolov-Ternov effect [5], photoionization of alkali atoms [6], the Fano effect [7], Mott scattering [8], and photoemission from a gallium arsenide (GaAs) cathode [9]. However, none of these conventional methods can generate the ultrashort (few microns long), high-current, and precisely synchronized

Published by the American Physical Society under the terms of the Creative Commons Attribution 4.0 International license. Further distribution of this work must maintain attribution to the author(s) and the published article's title, journal citation, and DOI.

(femtosecond) spin-polarized electron beams needed for injection into PBAs.

Recently, a down-ramp injection scheme using hydrogen halide gas to produce spin-polarized electrons in PBAs was proposed [10–12]. However, in this two-step scheme, multiple laser beams are needed to first produce a plasma with polarized electrons. Also, the prepolarized electrons can easily be depolarized in the down-ramp injection process, which limits both the accelerating gradient and charge of the injected electrons. In another proposal, a one-step scheme based on a spin-polarized ionization injection [13] suitable for a beam-driven plasma wakefield accelerator (PWFA) that uses a mixture of xenon and lithium was proposed. Unfortunately, this multispecies scheme is difficult to realize in practice, and in any case the spin polarization is limited to ~30%.

Here we show a simpler scheme that can achieve a higher degree of spin polarization at the same time. We propose to use a single atomic species, ytterbium, to act as a plasma photocathode [14,15] for both wake formation and ionization injection of spin-polarized electrons in a PWFA. Moreover, experimental demonstration of high-quality, highly spin-polarized electron beams is now possible through this scheme using state-of-the-art high-energy beam facilities such as the Facility for Advanced Accelerator Tests II (FACET-II) [16] at the SLAC National Accelerator Laboratory.

## II. PROPOSED SCHEME

The proposed scheme takes advantage of electron spin polarization resulting from the sensitivity of strong-field ionization of atoms or ions by intense circularly polarized laser

<sup>\*</sup>znie@ucla.edu

<sup>†</sup>lifei11@ucla.edu

<sup>‡</sup>cjoshi@ucla.edu

fields to the orbital angular momentum of initial bound orbitals [17–22]. Electrons removed from p, d, or f orbitals can form short spin-polarized bunches, while electrons removed from s orbitals are not spin polarized. We consider a Yb atom with the electron configuration [Xe]  $4f^{14}6s^2$ , with ionization potentials of the  $6s^2$ ,  $6s^1$ , and  $4f^{14}$  electrons being 6.25, 12.18, and 25.05 eV, respectively. Capitalizing on the significant difference in the ionization potentials for s and f electrons, we adjust the driving electron beam current such that its transverse electric field liberates primarily the two outer 6s electrons of Yb, leaving  $4f^{14}$  electrons largely bound. These two liberated but unpolarized 6s electrons and Yb<sup>2+</sup> ions form the plasma. If the driving electron bunch is ultrarelativistic  $(\gamma \gg 1)$  and sufficiently dense  $(n_b > n_p, k_p \sigma_{r,z} < 1)$ , then the plasma electrons are blown transversely by the collective Coulomb repulsion of the beam electrons to resonantly excite a bubblelike wake cavity [23], containing mostly the Yb<sup>2+</sup> (i.e., Yb III) ions. Here  $n_b$  and  $n_p$  are beam and plasma densities;  $k_p$ ,  $\sigma_r$ , and  $\sigma_z$  are the wave number of the linear wake, the rms bunch radius, and the bunch length, respectively. A 400 nm circularly polarized (CP) laser pulse, following the driving electron beam at a specific time delay, arrives at the position in the bubble where the on-axis longitudinal electric field of the wake is zero and liberates the outermost  $4f^{14}$  electrons of the Yb<sup>2+</sup> ions. These ionized spin-polarized electrons are then trapped near the rear of the first bucket of the wake and accelerated by the wake to multi-GeV energy.

# III. TIME-DEPENDENT SCHRÖDINGER EQUATION SIMULATIONS AND RESULTS

Theoretical advances and recent experiments on ionization of atoms in strong laser fields indicate that spin-polarized electrons can be produced by strong-field ionization because the ionization probability in CP fields depends on the sense of electron rotation (i.e., the magnetic quantum number  $m_l$ ) in the initial state [17–22]. This mechanism can operate for a broad range of laser frequencies and intensities. In our scheme (ionization of the f-orbital electrons of the Yb<sup>2+</sup> ions using a 400 nm CP laser), we operate in the nonadiabatic tunneling regime, where ionization of counterrotating electrons is dominant over that of corotating electrons. Using Yb<sup>2+</sup> yields a substantially higher degree of net spin polarization because f-orbital electrons in Yb<sup>2+</sup> have a higher angular momentum and hence stronger spin-orbit coupling [14,15] than lower-orbital (p or d) electrons in noble gases.

We use the time-dependent Schrödinger equation (TDSE) code SCID [24] for a range of laser intensities from  $2.8 \times 10^{13}$  to  $2.5 \times 10^{14}$  W/cm<sup>2</sup> for each ionization pathway to calculate the corresponding spin-up and spin-down electron ionization rates and yields [Fig. 1(a)]. The potentials have been modeled to describe the ionization of Yb<sup>2+</sup>, leaving the ion in a J=7/2 or a J=5/2 state. Energy of the 4f level in the J=7/2 channel was set at the experimental ionization potential of 25.053 eV [25]. The experimental spin-orbit splitting of 1.26637 eV [26] was used to set the 4f level in the J=5/2 channel. Experimental atomic excitation energies were taken from Ref. [26] and supplemented with theoretical

results from Ref. [27]. The effective potentials in the modified form [28] (atomic units) are

$$u(r) = \infty \quad (r \leqslant r_{\min}),$$
 (1)

$$u(r) = -\frac{3}{r} + \frac{a}{r} \frac{1}{b + \frac{d}{c}[\exp(cr) - 1]} \quad (r > r_{\min}). \quad (2)$$

The fit parameters for J = 7/2 and J = 5/2 states are summarized in Table I. More details about TDSE simulations are given in Sec. A 1.

Here we choose right-handed CP laser pulses in our TDSE simulations, and we define spin polarization as  $(N_{\uparrow} N_{\downarrow})/(N_{\uparrow}+N_{\downarrow})$ , where  $N_{\uparrow,\downarrow}$  represents the number of spin-up or spin-down (parallel or antiparallel to laser wave vector  $\vec{k}$ ) electrons. From TDSE simulations, the maximum ionization degrees of spin-up and spin-down electrons versus laser intensity are shown in Fig. 1(a). Accordingly, the net spin polarization after integration over the entire temporal and spatial intensity distribution of the laser pulse, all photoelectron energies, and all final ionic states is shown in Fig. 1(b). From Fig. 1(b), we can see that the net spin polarization can be higher than 50% for a broad range of laser intensity  $(0.8-2.5)\times10^{14}$  W/cm<sup>2</sup> after focal-volume averaging. Therefore, the injected electron charge can be increased (decreased) by increasing (decreasing) the laser intensity in this range while not appreciably changing the degree of spin polarization. The steep drop in spin polarization at  $\sim 0.5 \times 10^{14} \text{ W/cm}^2$ is due to the Freeman resonances [29]. The r-z spatial distributions of the total ionization fraction and spin polarization at a laser intensity of  $1.18 \times 10^{14} \text{ W/cm}^2$  [which will be used in the later particle-in-cell (PIC) simulations] are shown in Figs. 1(c) and 1(d), respectively. From Fig. 1(c), we can see that the maximum ionization fraction of the  $4f^{14}$  electrons of Yb is about 19%. In Fig. 1(d), a dark red half ellipse representing low spin polarization at  $\sim 0.5 \times 10^{14} \text{ W/cm}^2$  due to the Freeman resonance mentioned above is clearly observed, but the ionization yield of these electrons is low ( $<10^{-3}$ ), so that the net spin polarization can still reach 56% after focal-volume averaging.

## IV. PIC SIMULATIONS AND RESULTS

Next, we incorporate the spin-dependent ionization results into the wakefield acceleration simulations using OSIRIS [30,31] and QPAD [32] codes. More details are shown in Appendix A 2 and A 3. We have implemented the spin precession module into both the OSIRIS and QPAD codes following the Thomas–Bargmann-Michel-Telegdi equation [33]:

$$d\mathbf{s}/dt = \mathbf{\Omega} \times \mathbf{s},\tag{3}$$

where  $\mathbf{\Omega} = \frac{e}{m}(\frac{1}{\gamma}\mathbf{B} - \frac{1}{\gamma+1}\frac{\mathbf{v}}{c^2}\times\mathbf{E}) + a_e\frac{e}{m}[\mathbf{B} - \frac{\gamma}{\gamma+1}\frac{\mathbf{v}}{c^2}(\mathbf{v}\cdot\mathbf{B}) - \frac{\mathbf{v}}{c^2}\times\mathbf{E}]$ . Here  $\mathbf{E}$  and  $\mathbf{B}$  are the electric and magnetic fields,  $\mathbf{v}$  is the electron velocity,  $\gamma = \frac{1}{\sqrt{1-v^2/c^2}}$  is the relativistic factor, and  $a_e \approx 1.16\times10^{-3}$  is the anomalous magnetic moment of the electron.

We carried out numerous PIC simulations in which the parameters of the driving electron beam and ionizing laser were varied. Here we present results for parameters which gave the best results but note that further optimization is

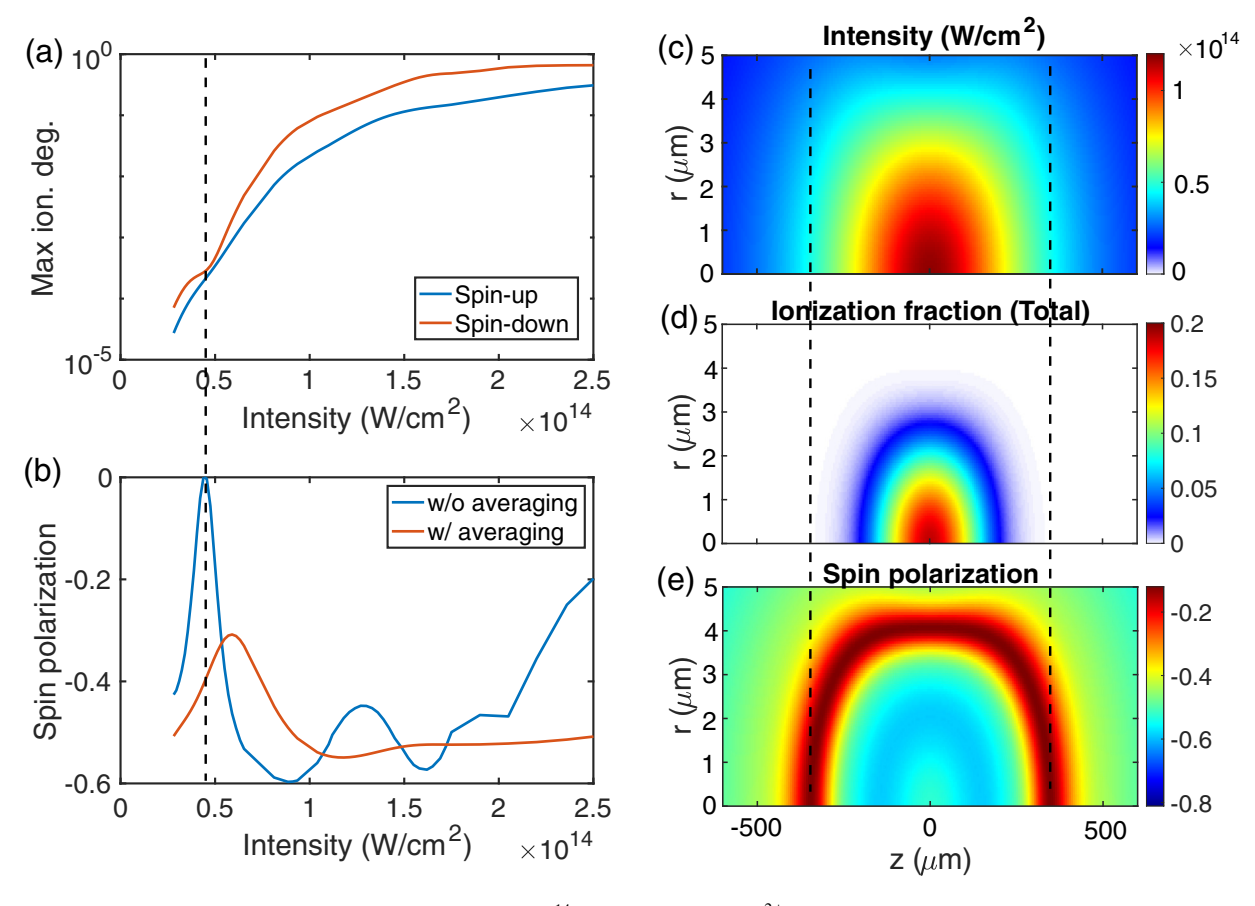


FIG. 1. TDSE simulation results for ionization of the  $4f^{14}$  electron of the Yb<sup>2+</sup> ion. (a) Maximum ionization degree of spin-up and spin-down electrons as a function of the laser peak intensity of a 400 nm, 60 fs (FWHM), right-handed CP laser that ionizes spin-down electrons preferentially. (b) Spin polarization (on axis) as a function of peak laser intensity without (blue; 1D) and with (red; 3D) focal-volume averaging in the region of  $r < w_0$  and |z| < Rayleigh length. The dashed line in (a) and (b) corresponds to the dip of spin polarization at  $\sim 0.5 \times 10^{14}$  W/cm<sup>2</sup>. (c)–(e) The laser intensity distribution, total ionization fraction distribution, and spin polarization distribution in the r-z-z-plane for a bi-Gaussian 60 fs (FWHM),  $w_0 = 6.0 \ \mu m$ , 400 nm laser with a peak intensity of  $1.18 \times 10^{14}$  W/cm<sup>2</sup>. The two dashed lines in (c)–(e) correspond to the same on-axis laser intensity as the dashed line in (a) and (b).

possible. The driving electron beam has a Gaussian profile  $n_b = \frac{N}{(2\pi)^{\frac{3}{2}} \sigma_r^2 \sigma_z} \exp(-\frac{r^2}{2\sigma_r^2} - \frac{\xi^2}{2\sigma_z^2})$ , where  $N = 7.5 \times 10^9$  (1.2 nC) and  $\sigma_r = 6.4 \, \mu \text{m}$  and  $\sigma_z = 12.7 \, \mu \text{m}$  are the transverse and longitudinal beam sizes, respectively. The driving electron beam energy is 10 GeV with a normalized emittance of  $\epsilon_n = 16 \, \mu \text{m}$ . The transverse electric field of a relativistic electron beam with a Gaussian profile can be expressed as

$$E_r = \frac{1}{(2\pi)^{\frac{3}{2}}} \frac{e}{\epsilon_0} \frac{N}{\sigma_r \sigma_z} \frac{1 - \exp\left(-\frac{r^2}{2\sigma_r^2}\right)}{r/\sigma_r} \exp\left(-\frac{z^2}{\sigma_z^2}\right). \tag{4}$$

Such a transverse electric field vanishes at r=0 and has a maximum [34]  $E_r^{\rm max}=10.4\frac{N}{10^{10}}\frac{10}{\sigma_r[\mu{\rm m}]}\frac{50}{\sigma_z[\mu{\rm m}]}$  [GV/m] at  $r\approx 1.6\sigma_r$ . When such a beam enters into very low density neutral gases, it cannot ionize gas near the r=0 axis. However, in

TABLE I. Effective-potential fit parameters.

J	$r_{ m min}$	а	b	с	d
7/2			1.0	0.25477	-9.9480672
5/2	0.161705	47.9445593	1.0	0.25019	-10.3512619

the simulations, the on-axis atoms are seen to be ionized by a combination of the transverse fields of the wake and the electric field of the driving beam (which can be enhanced due to self-focusing in the wake). In our simulations, the Yb gas has a uniform density of  $n_{Yb} = 5.22 \times 10^{16}$  cm<sup>-3</sup> with an up-ramp length of 100  $\mu m$  (shorter than experimental values to save simulation time). In reality, if the ramp is about 10 cm long, the focus of the driving beam can be moved accordingly so that it does not pinch in the ramp [16]. By choosing such Yb gas density and driving beam parameters, we can get a large enough region around the axis  $(r < 7 \,\mu\text{m})$  where the two 6s electrons of Yb are fully ionized [Fig. 2(c)]. It is this region that the follow-up ionizing laser can further ionize Yb<sup>2+</sup> to generate spin-polarized beams. At around  $r \approx 1.6\sigma_r \approx 10 \,\mu\text{m}$ , a small fraction of the third electron ( $4f^{14}$  electron) of Yb is also ionized, but they are also blown out by the driving beam, as shown in Fig. 2(c), and are not subsequently trapped. We note that at this early stage the ionization of the third electron is not caused by the pinching of the driving beam that occurs later from self-focusing. The driving electron beam blows out the first two and some of the third ionized electrons to create the wake cavity, leaving the remaining Yb<sup>2+</sup> ions around the axis. The 400 nm ionization

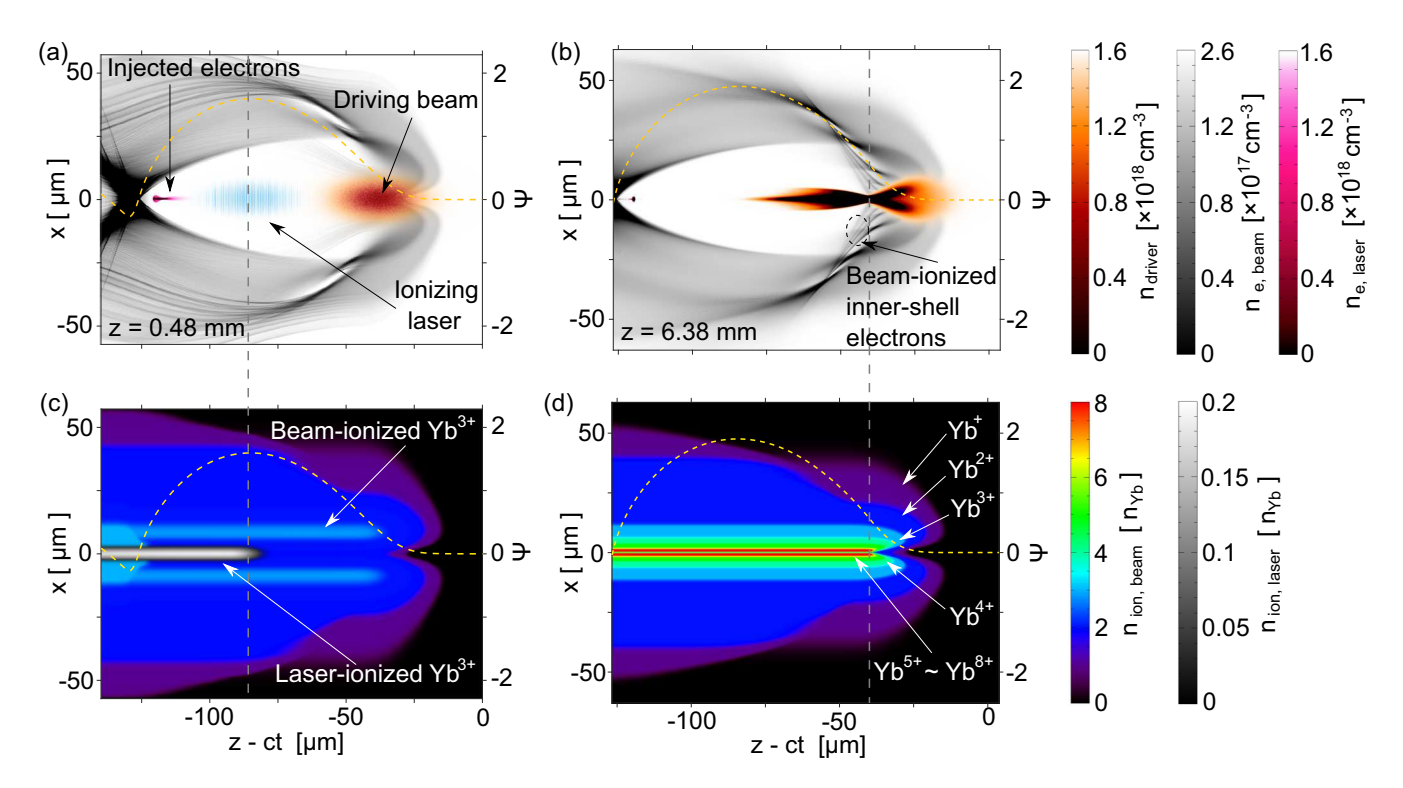


FIG. 2. Snapshots of ionization injection and acceleration. Two snapshots show the charge density distribution of the driving electron beam (brown), beam-ionized Yb electrons (gray), and laser-ionized  $4f^{14}$  electrons of Yb (purple) at (a) z=0.48 mm (at around laser focus) and (b) z=6.38 mm (driving beam pinched). (c) and (d), The Yb ion charge density distribution at the same moment as in (a) and (b), respectively. The yellow dashed lines in (a)–(d) show the on-axis wake pseudopotential. (a) and (c) are from OSIRIS simulations. (b) and (d) are from QPAD simulations. (see the Appendix).

laser with a pulse duration (FWHM) of 60 fs and focal spot size of  $w_0 = 6.0 \, \mu \text{m}$  is delayed by 156 fs (46.7  $\mu \text{m}$ ) from the peak current position of the driving electron beam. This delay is chosen so that the laser is at the center of the wake bubble [Fig. 2(a)] and hence the best trapping condition is achieved  $[\Delta \Psi = \Psi_f - \Psi_i \leqslant -1]$ , where  $\Psi = e/(mc^2)(\phi - A_z)$  is the normalized pseudopotential of the wake and subscripts i and f indicate the value of the pseudopotential at the position of ionization and trapping, respectively] [35]. Here  $\phi$  is the electric potential, and  $A_z$  is the longitudinal component of the vector potential. The peak laser intensity is  $1.18 \times 10^{14} \, \text{W/cm}^2$  [the same intensity as in Figs. 1(c) and 1(d)].

As the unmatched (plasma ion focusing force greater than the diffraction caused by the beam emittance) driving electron beam propagates in the plasma, it is seen to pinch [36], leading to stronger local electric field and ionization of multiple 4f orbital electrons of Yb, as shown in Figs. 2(b) and 2(d). Up to eight electrons can be ionized by the pinched driving electron beam, but these extra ionized electrons are not trapped and accelerated by the wakefield (beam-induced ionization injection [37,38]) because the pulse length of our driving beam is short compared to the plasma cavity length; the location of beam-induced ionization is at the head of the wake where the difference between the initial and final pseudopotentials  $\Delta\Psi$ is not sufficient to satisfy the trapping condition. To verify this, we have run another PIC simulation (using quasi-3D OSIRIS [39,40] to save simulation time) with the same parameters but without the ionizing laser, and we found that no self-injection occurs in this case; that is, no dark current exists. We have tried using a driving electron beam with larger emittances or smaller spot sizes to minimize self-focusing. For larger emittances, the head of the beam diffracts, preventing multi-GeV energy gain. For narrower spot sizes, the drive beam ionizes Yb<sup>2+</sup> closer to the axis such that the column of the Yb<sup>2+</sup> is too narrow and some of the unpolarized electrons get trapped. Therefore, the parameters we used here are a trade-off result between these two issues.

Evolution of injected beam parameters, including charge, peak current, and spin vector distribution, as a function of propagation distance in the plasma is shown in Fig. 3. Photoionized electrons with a charge of 5.3 pC [Fig. 3(a), left axis] are injected, trapped, and accelerated to 15 GeV [Fig. 3(b)] in 41 cm until the driving beam is depleted of its energy. The pulse length of the injected bunch first increases to about  $\sigma_{zi} = 10 \,\mu\text{m}$  and then decreases to a final pulse length of only  $\sigma_{zf} = 0.2 \,\mu\text{m}$  at the very back of the wake, corresponding to a subfemtosecond bunch [41]. The peak current is as high as 4 kA [Fig. 3(a), right axis], and the final normalized emittance is  $\epsilon_n = 180$  nm. The spin vector evolutions in the z directions are shown in Fig. 3(c). The spin spread in the transverse (x or y) direction is symmetric so that  $\langle s_x \rangle \approx \langle s_y \rangle \approx 0$ . Therefore, the net spin polarization  $P = P_z = \langle s_z \rangle$  depends on only the spin distribution in the z direction. The final averaged spin polarization is  $\langle s_z \rangle = 56\%$  [Fig. 3(c)] with almost no depolarization during injection and acceleration processes.

## V. DISCUSSION

In our scheme, good control of the delay and alignment between the driving beam and ionizing CP laser pulse is

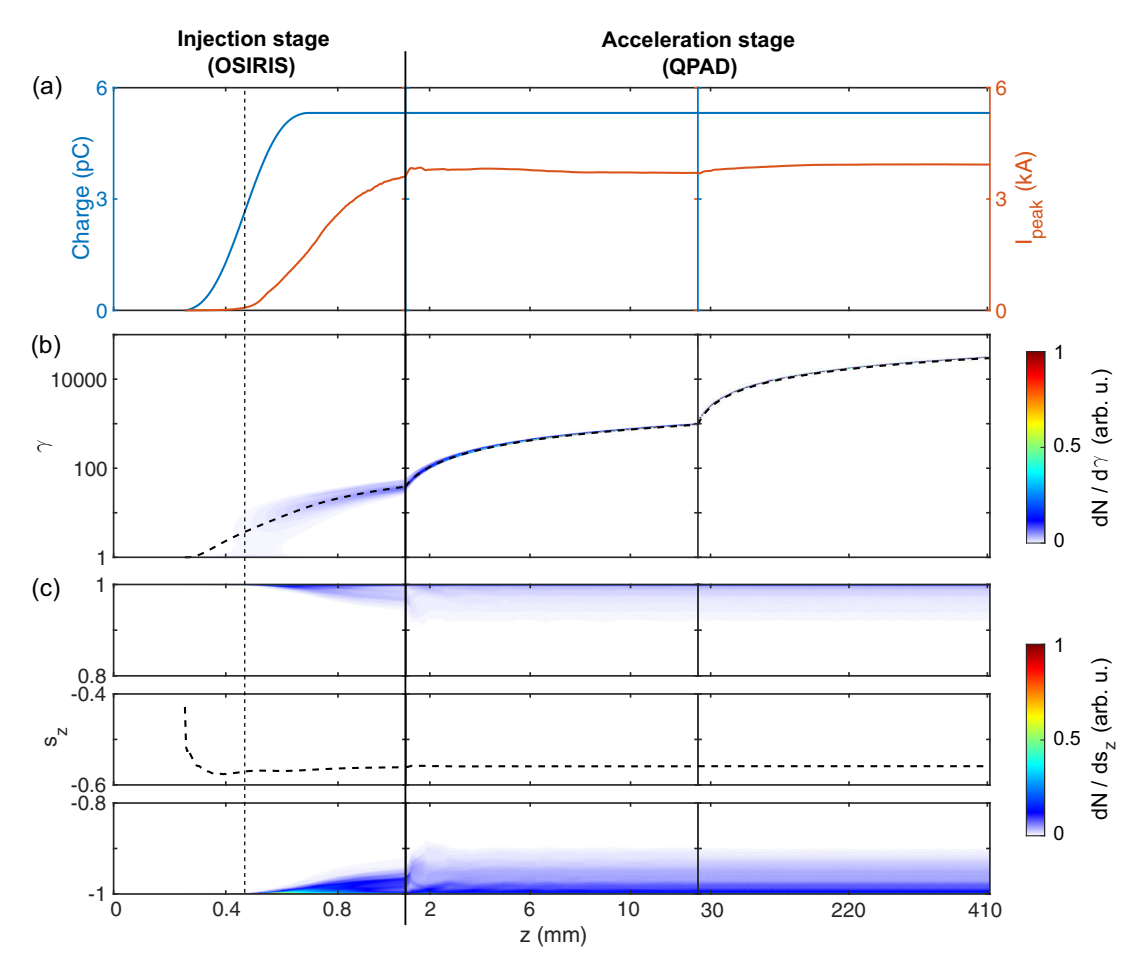


FIG. 3. Evolution of injected electrons as a function of the propagating distance. (a) Evolution of the beam charge (left axis) and peak current (right axis). (b) Evolution of the Lorentz factor  $\gamma$ . The dashed line presents mean energy  $\langle \gamma \rangle$ . (c) Evolution of the spin vector in the z direction  $s_z$ . The top box plots the  $s_z$  distribution in the range of 0.8 and 1, corresponding to spin-up electron density. The middle box plots  $\langle s_z \rangle$  (net spin polarization) in the range of -0.6 to -0.4. The bottom box plots the  $s_z$  distribution in the range of -1 to -0.8, corresponding to spin-down electron density. The long vertical dashed black line marks the focal position (z = 0.47 mm) of the ionization laser. The apparent discontinuities at the boundaries of different stages are not real and appear only because the horizontal scale changes between different stages.

crucial, but it can be achieved using state-of-the-art techniques. The relative timing jitter should be controlled within tens of femtoseconds to maintain a stable beam charge and emittance. Such stringent control on the temporal jitter between a femtosecond laser pulse and the radio-frequency power source that produces the electron beam was recently achieved in Refs. [42–45]. Nowadays, the angular pointing of a laser beam can be stabilized within submicroradian level using state-of-the-art active stabilization techniques [46–50], which correspond to a submicron level of transverse offset fluctuation at focus with a focal length of 1 m. We find that for the conditions of our simulation case, a transverse offset as large as 3  $\mu$ m still yields the same spin polarization but the normalized emittance in the offset direction becomes twice that in the other direction. Therefore, the pointing jitter is not thought to be a problem.

Finally, we wish to point out that the temperature dependence of the vapor pressure of Yb is very similar to that of Li; thus, it should be no more difficult to make a long homogeneous column of Yb vapor than it would be for Li, which has been used with great success in the past two decades [51],

making the realizability of this idea promising in the near future with available facilities such as FACET II.

## VI. CONCLUSION

In summary, we have proposed a scheme to produce a high-degree spin-polarized subfemtosecond electron beam using strong-field ionization of the Yb<sup>2+</sup> ions by a CP laser pulse inside a plasma photocathode. Using a single atomic species to both excite the plasma wake and be the source of spin-polarized electrons for injection makes this concept experimentally realizable, thus solving a long-standing problem facing the development of plasma-based accelerators.

## **ACKNOWLEDGMENTS**

This work was supported by U.S. Department of Energy (DOE) Grant No. DE-SC0010064; DOE through a SciDAC FNAL Subcontract No. 644405; the National Science Foundation (NSF) Grants No. 1734315, No. 1806046, and No. 2108970; the Office of Naval Research (ONR) Multidisciplinary University Research Initiative (MURI)

(4-442521-JC-22891); and the National Natural Science Foundation of China (NSFC) Grant No. 12075030. The simulations were performed on Hoffman cluster at UCLA and the computing resources of the National Energy Research Scientific Computing Center (NERSC).

#### **APPENDIX**

#### 1. Details of TDSE simulations

The degree of spin polarization was calculated solving the TDSE in the presence of two different single active electron potentials, using the SCID code [24]. The potentials have been modeled to describe the ionization of Yb<sup>2+</sup>, leaving the ion in a J = 7/2 or a J = 5/2 state. The parameters have been fitted to the multiplet centers of mass. The summary in Ref. [26] and fitted energies relative to the 4f ground-state level are given in Tables II and III, respectively, for the J = 7/2 and J = 5/2 cores. By adding the hard boundary to the potential, we exclude the deep 1s, 2s, and 2p levels. We furthermore do not constrain the positions of the inner levels (3s, 3p, 3d, 4s,4p, 4d, 5s, 5p) in the fit. These levels are never significantly populated in our TDSE simulations.

We have performed the simulations in a box of 189.17 a.u., using a nonuniform grid, starting with a 37-point uniform grid, from 0.16 to 1.95 a.u., followed by a 57-point logarithmic grid with a scaling parameter of 1.025, starting at 2.0 a.u., and ending with a 906-point uniform grid with a spacing of 0.2 a.u from 8.17 a.u. In order to avoid nonphysical reflections from the edges of the box, we have placed a complex absorbing potential [52] at a distance of 156.77 a.u. from the origin, with a width of 32.8 a.u. We have included up to l, |m| = 60angular channels for the angular part of the wave function. We have used a right-handed CP laser pulse, with a Gaussian envelope, and a FWHM of 10 fs, with a carrier of 400 nm (3.0996 eV). The time coordinate was discretized with a time step of dt = 0.002 a.u.

Simulations were done starting from each of the possible seven f initial states of Yb III (l = 3, m = -3 to m = 3), which leads to 14 simulations for each intensity point. Ionization rates as a function of intensity were calculated using the ionization probability of each channel. Summing up the ionization rates from all these different channels based on the Clebsch-Gordan coefficients [15], we can get the ionization rates of the spin-up or spin-down electrons in J = 7/2 and J = 5/2 states and then get the total ionization rates of spin-up and spin-down electrons.

TABLE II. Level positions for the J = 7/2 core. The span of the level is the largest distance between the experimental multiplets. Reference (ref) data are from Ref. [26].

Level	Position, ref (eV)	Position, fit (eV)	Span, ref (eV)
6 <i>s</i>	-20.738	-20.953	0.041
7 <i>s</i>	-10.138	-10.220	0.014
6 <i>p</i>	-15.570	-15.901	0.886
7p	-7.992	-8.269	0.305
5 <i>d</i>	-20.092	-19.311	1.270
6 <i>d</i>	-9.306	-9.220	0.305
4f	-25.053	-25.054	

TABLE III. Level positions for the J = 5/2 core. The span of the level is the largest distance between the experimental multiplets. Reference (ref) data are from Ref. [26].

Level	Position, ref (eV)	Position, fit (eV)	Span, ref (eV)
6 <i>s</i>	-20.732	-20.926	0.044
7 <i>s</i>	-10.138	-10.217	0.011
6 <i>p</i>	-15.566	-15.911	0.850
7p	-8.216	-8.275	0.303
5 <i>d</i>	-20.019	-19.397	1.048
6 <i>d</i>	-9.516	-9.253	0.494
4 <i>f</i>	-26.319	-26.318	

## 2. Implementing the TDSE ionization model into the PIC code

To incorporate TDSE and PIC simulations, we implemented a TDSE ionization model specified for photoionization of Yb<sup>2+</sup> ions in the PIC code. This TDSE ionization model is based on a series of off-line TDSE simulations carried out to obtain the ionization rates of both spin-up and spin-down electrons in the range of laser intensities of interest [Fig. 1(a)]. The local photoionization rates of Yb<sup>2+</sup> ions in the PIC simulations are obtained via table lookup and interpolation. A certain number of macroparticles representing ionized electrons with a specific spin polarization distribution will be released according to the transient yields of spin-up and spin-down electrons. The densities of  $Yb^{2+}$  ions  $(N_0)$  and of Yb<sup>3+</sup> ions that have released spin-up  $(N_{\uparrow})$  and spin-down  $(N_{\perp})$  electrons are numerically solved through the following rate equations:

$$\frac{dN_0}{dt} = -(w^{\uparrow} + w^{\downarrow})N_0, \tag{A1}$$

$$\frac{dN_{\uparrow}}{dt} = w^{\uparrow}N_0, \tag{A2}$$

$$\frac{dN_{\uparrow}}{dt} = w^{\uparrow} N_0, \tag{A2}$$

$$\frac{dN_{\downarrow}}{dt} = w^{\downarrow} N_0, \tag{A3}$$

where  $w^{\uparrow,\downarrow}$  represents the ionization rate of spin-up or spindown electrons.

#### 3. Details of the PIC simulations

The start-to-end PIC simulations consisting of two stages were carried out using the full 3D code OSIRIS [30,31] and the quasistatic code QPAD [32]. For each stage, the simulation window moving at the speed of light moves along the z axis, i.e., the propagation direction of the driving beam and ionizing laser pulse. Ions are assumed to not be moving in our simulations.

We used OSIRIS in the first stage (the injection stage) to model the photoionization, particle injection, and spin precession at early times. We used the Ammosov-Delone-Krainov (ADK) ionization model [53] to calculate the ionization induced by the driving electron beam and the TDSE ionization model to calculate the spin-dependent photoionization rates of Yb<sup>2+</sup> ions induced by the ionizing laser. In our simulations, we always make sure that the driving electron beam fully ionizes the first two electrons but not the third electron of Yb near the focus of the ionizing laser. In other words, we always make sure the ionizing laser interacts only with Yb<sup>2+</sup> ions. Only in this way can we use two ionization models separately. The simulation window had dimensions of  $114\times114\times153\,\mu\text{m}^3$  in the  $x,\,y,$  and z directions, respectively. We used  $450\times450\times1200$  cells in the corresponding directions. Together with the selected time step of 0.3 fs, the space-time resolution is sufficient to model the early-time laser photoionization, the trapping of the  $4f^{14}$  electrons, and their subsequent phase space evolution and spin precession. The number of macroparticles of Yb per cell was 32. The injected electrons were accelerated to ultrarelativistic energy ( $\gamma \sim 20$ ) until they were extracted and used as inputs for the second stage (the acceleration stage).

In the second stage, where the ionization injection has ceased, the trapped electron beam undergoes acceleration by the essentially nonevolving plasma wake. The quasistatic approximation [54] is valid in the absence of particle injection, and thus, the quasistatic code QPAD was employed to explore the physics therein. Therefore, the TDSE ionization model is not included any more, but we still use the ADK ionization model to calculate the ionization induced by the driving electron beam. Benefiting from the speedup techniques in QPAD, a long-distance (time) simulation with much finer resolution for a lower cost of computational resources is achievable. The moving simulation window has dimensions of  $57 \times 153 \, \mu \text{m}^2$  in the radial and propagation directions, with  $3200 \times 3200$  cells in the corresponding directions. Since the selection of the time step in a quasistatic code is not subject to the numerical stability consideration, a much larger time step of 78 fs is chosen to resolve the betatron oscillation of beam particles.

- B. Barish and J. E. Brau, The international linear collider, Int. J. Mod. Phys. A 28, 1330039 (2013).
- [2] P. Souder and K. D. Paschke, Parity violation in electron scattering, Front. Phys. 11, 111301 (2016).
- [3] D. Adhikari *et al.* (PREX Collaboration), Accurate Determination of the Neutron Skin Thickness of <sup>208</sup>Pb through Parity-Violation in Electron Scattering, Phys. Rev. Lett. 126, 172502 (2021).
- [4] C. Joshi, New ways to smash particles, Scientific American, 55 (2021).
- [5] A. Sokolov and I. Ternov, On polarization and spin effects in the theory of synchrotron radiation, Sov. Phys. Dokl. 8, 1203 (1964).
- [6] R. L. Long, W. Raith, and V. W. Hughes, Polarized Electrons from a Polarized Atomic Beam, Phys. Rev. Lett. 15, 1 (1965).
- [7] U. Fano, Spin orientation of photoelectrons ejected by circularly polarized light, Phys. Rev. **178**, 131 (1969).
- [8] H. Tolhoek, Electron polarization, theory and experiment, Rev. Mod. Phys. 28, 277 (1956).
- [9] D. T. Pierce and F. Meier, Photoemission of spin-polarized electrons from gaas, Phys. Rev. B 13, 5484 (1976).
- [10] M. Wen, M. Tamburini, and C. H. Keitel, Polarized Laser-Wakefield-Accelerated Kiloampere Electron Beams, Phys. Rev. Lett. 122, 214801 (2019).
- [11] Y. Wu, L. Ji, X. Geng, Q. Yu, N. Wang, B. Feng, Z. Guo, W. Wang, C. Qin, X. Yan, L. Zhang, J. Thomas, A. Hützen, A. Pukhov, M. Büscher, B. Shen, and R. Li, Polarized electron acceleration in beam-driven plasma wakefield based on density down-ramp injection, Phys. Rev. E 100, 043202 (2019).
- [12] Y. Wu, L. Ji, X. Geng, Q. Yu, N. Wang, B. Feng, Z. Guo, W. Wang, C. Qin, X. Yan, L. Zhang, J. Thomas, A. Hützen, M. Büscher, T. P. Rakitzis, A. Pukhov, B. Shen, and R. Li, Polarized electron-beam acceleration driven by vortex laser pulses, New J. Phys. 21, 073052 (2019).
- [13] Z. Nie, F. Li, F. Morales, S. Patchkovskii, O. Smirnova, W. An, N. Nambu, D. Matteo, K. A. Marsh, F. Tsung, W. B. Mori, and C. Joshi, *In Situ* Generation of High-Energy Spin-Polarized Electrons in a Beam-Driven Plasma Wakefield Accelerator, Phys. Rev. Lett. 126, 054801 (2021); 127, 269901(E) (2021).
- [14] J. Kaushal and O. Smirnova, Looking inside the tunnelling barrier: I. Strong field ionisation from orbitals with high angular

- momentum in circularly polarised fields, J. Phys. B **51**, 174001 (2018).
- [15] J. Kaushal and O. Smirnova, Looking inside the tunnelling barrier III: Spin polarisation in strong field ionisation from orbitals with high angular momentum, J. Phys. B 51, 174003 (2018).
- [16] C. Joshi, E. Adli, W. An, C. E. Clayton, S. Corde, S. Gessner, M. J. Hogan, M. Litos, W. Lu, K. A. Marsh, W. B. Mori, N. Vafaei-Najafabadi, B. O'Shea, X. Xu, G. White, and V. Yakimenko, Plasma wakefield acceleration experiments at FACET II, Plasma Phys. Controlled Fusion 60, 034001 (2018).
- [17] I. Barth and O. Smirnova, Spin-polarized electrons produced by strong-field ionization, Phys. Rev. A 88, 013401 (2013).
- [18] A. Hartung, F. Morales, M. Kunitski, K. Henrichs, A. Laucke, M. Richter, T. Jahnke, A. Kalinin, M. Schöffler, L. P. H. Schmidt, M. Ivanov, O. Smirnova, and R. Dörner, Electron spin polarization in strong-field ionization of xenon atoms, Nat. Photon. 10, 526 (2016).
- [19] I. Barth and O. Smirnova, Nonadiabatic tunneling in circularly polarized laser fields. II. Derivation of formulas, Phys. Rev. A 87, 013433 (2013).
- [20] T. Herath, L. Yan, S. K. Lee, and W. Li, Strong-Field Ionization Rate Depends on the Sign of the Magnetic Quantum Number, Phys. Rev. Lett. 109, 043004 (2012).
- [21] S. Eckart, M. Kunitski, M. Richter, A. Hartung, J. Rist, F. Trinter, K. Fehre, N. Schlott, K. Henrichs, L. P. H. Schmidt et al., Ultrafast preparation and detection of ring currents in single atoms, Nat. Phys. 14, 701 (2018).
- [22] Y. Trabert, L. Ji, X. Geng, Q. Yu, N. Wang, B. Feng, Z. Guo, W. Wang, C. Qin, X. Yan, L. Zhang, J. Thomas, A. Hutzen, A. Pukhov, M. Buscher, B. Shen, and R. Li, Spin and Angular Momentum in Strong-Field Ionization, Phys. Rev. Lett. 120, 043202 (2018).
- [23] W. Lu, C. Huang, M. Zhou, W. B. Mori, and T. Katsouleas, Nonlinear Theory for Relativistic Plasma Wakefields in the Blowout Regime, Phys. Rev. Lett. 96, 165002 (2006).
- [24] S. Patchkovskii and H. Muller, Simple, accurate, and efficient implementation of 1-electron atomic time-dependent Schrödinger equation in spherical coordinates, Comput. Phys. Commun. 199, 153 (2016).
- [25] D. R. Lide, CRC Handbook of Chemistry and Physics, 82nd ed. (CRC Press, Boca Raton, FL, 2005).

- [26] A. Kramida, Yu. Ralchenko, J. Reader, and NIST ASD Team, NIST Atomic Spectra Database, version 5.9, https://physics. nist.gov/asd.
- [27] U. I. Safronova and M. S. Safronova, Correlation and relativistic effects for the 4*f-nl* multipole transitions in Yb III ions, Phys. Rev. A **79**, 032511 (2009).
- [28] R. H. Garvey, C. H. Jackman, and A. E. S. Green, Independent-particle-model potentials for atoms and ions with  $36 < z \le 54$  and a modified Thomas-Fermi atomic energy formula, Phys. Rev. A **12**, 1144 (1975).
- [29] R. R. Freeman, P. H. Bucksbaum, H. Milchberg, S. Darack, D. Schumacher, and M. E. Geusic, Above-threshold ionization with subpicosecond laser pulses, Phys. Rev. Lett. 59, 1092 (1987).
- [30] R. A. Fonseca, L. O. Silva, F. S. Tsung, V. K. Decyk, W. Lu, C. Ren, W. B. Mori, S. Deng, S. Lee, T. Katsouleas, and J. C. Adam, OSIRIS: A three-dimensional, fully relativistic particle in cell code for modeling plasma based accelerators, in *Computational Science—ICCS 2002*, edited by P. M. A. Sloot, A. G. Hoekstra, C. J. K. Tan, and J. J. Dongarra (Springer, Berlin, Heidelberg, 2002), pp. 342–351.
- [31] R. Fonseca, S. Martins, L. Silva, J. Tonge, F. Tsung, and W. Mori, One-to-one direct modeling of experiments and astrophysical scenarios: Pushing the envelope on kinetic plasma simulations, Plasma Phys. Controlled Fusion 50, 124034 (2008).
- [32] F. Li, W. An, V. K. Decyk, X. Xu, M. J. Hogan, and W. B. Mori, A quasi-static particle-in-cell algorithm based on an azimuthal fourier decomposition for highly efficient simulations of plasma-based acceleration: Qpad, Comput. Phys. Commun. 261, 107784 (2021).
- [33] V. Bargmann, L. Michel, and V. L. Telegdi, Precession of the Polarization Particles Moving a Homogeneous Electromagnetic Field, Phys. Rev. Lett. **2**, 435 (1959).
- [34] C. L. O'Connell, C. D. Barnes, F.-J. Decker, M. J. Hogan, R. Iverson, P. Krejcik, R. Siemann, D. R. Walz, C. E. Clayton, C. Huang, D. K. Johnson, C. Joshi, W. Lu, K. A. Marsh, W. Mori, M. Zhou, S. Deng, T. Katsouleas, P. Muggli, and E. Oz, Plasma production via field ionization, Phys. Rev. Spec. Top. Accel. Beams 9, 101301 (2006).
- [35] A. Pak, K. A. Marsh, S. F. Martins, W. Lu, W. B. Mori, and C. Joshi, Injection and Trapping of Tunnel-Ionized Electrons into Laser-Produced Wakes, Phys. Rev. Lett. 104, 025003 (2010).
- [36] X. L. Xu, J. F. Hua, Y. P. Wu, C. J. Zhang, F. Li, Y. Wan, C.-H. Pai, W. Lu, W. An, P. Yu, M. J. Hogan, C. Joshi, and W. B. Mori, Physics of Phase Space Matching for Staging Plasma and Traditional Accelerator Components Using Longitudinally Tailored Plasma Profiles, Phys. Rev. Lett. 116, 124801 (2016).
- [37] E. Oz *et al.*, Ionization-Induced Electron Trapping in Ultrarelativistic Plasma Wakes, Phys. Rev. Lett. **98**, 084801 (2007).
- [38] N. Vafaei-Najafabadi et al., Producing multi-coloured bunches through beam-induced ionization injection in plasma wakefield accelerator, Philos. Trans. R. Soc. A 377, 20180184 (2019).
- [39] A. Lifschitz, X. Davoine, E. Lefebvre, J. Faure, C. Rechatin, and V. Malka, Particle-in-cell modelling of laser-plasma interaction using Fourier decomposition, J. Comput. Phys. 228, 1803 (2009).
- [40] A. Davidson, A. Tableman, W. An, F. Tsung, W. Lu, J. Vieira, R. Fonseca, L. Silva, and W. Mori, Implementation of a hy-

- brid particle code with a PIC description in rz and a gridless description in  $\phi$  into OSIRIS, J. Comput. Phys. **281**, 1063 (2015).
- [41] X. L. Xu, C.-H. Pai, C. J. Zhang, F. Li, Y. Wan, Y. P. Wu, J. F. Hua, W. Lu, W. An, P. Yu, C. Joshi, and W. B. Mori, Nanoscale Electron Bunching in Laser-Triggered Ionization Injection in Plasma Accelerators, Phys. Rev. Lett. 117, 034801 (2016).
- [42] R. Pompili, M. Anania, M. Bellaveglia, A. Biagioni, G. Castorina, E. Chiadroni, A. Cianchi, M. Croia, D. Di Giovenale, M. Ferrario *et al.*, Femtosecond timing-jitter between photocathode laser and ultra-short electron bunches by means of hybrid compression, New J. Phys. 18, 083033 (2016).
- [43] H.-S. Kang, C.-K. Min, H. Heo, C. Kim, H. Yang, G. Kim, I. Nam, S. Y. Baek, H.-J. Choi, G. Mun *et al.*, Hard x-ray free-electron laser with femtosecond-scale timing jitter, Nat. Photon. 11, 708 (2017).
- [44] E. C. Snively, M. A. K. Othman, M. Kozina, B. K. Ofori-Okai, S. P. Weathersby, S. Park, X. Shen, X. J. Wang, M. C. Hoffmann, R. K. Li, and E. A. Nanni, Femtosecond Compression Dynamics and Timing Jitter Suppression in a THz-Driven Electron Bunch Compressor, Phys. Rev. Lett. 124, 054801 (2020).
- [45] L. Zhao, H. Tang, C. Lu, T. Jiang, P. Zhu, L. Hu, W. Song, H. Wang, J. Qiu, C. Jing, S. Antipov, D. Xiang, and J. Zhang, Femtosecond Relativistic Electron Beam with Reduced Timing Jitter from THz Driven Beam Compression, Phys. Rev. Lett. 124, 054802 (2020).
- [46] A. R. Maier, N. M. Delbos, T. Eichner, L. Hubner, S. Jalas, L. Jeppe, S. W. Jolly, M. Kirchen, V. Leroux, P. Messner, M. Schnepp, M. Trunk, P. A. Walker, C. Werle, and P. Winkler, Decoding Sources of Energy Variability in a Laser-Plasma Accelerator, Phys. Rev. X 10, 031039 (2020).
- [47] T. Kanai, A. Suda, S. Bohman, M. Kaku, S. Yamaguchi, and K. Midorikawa, Pointing stabilization of a high-repetition-rate high-power femtosecond laser for intense few-cycle pulse generation, Appl. Phys. Lett. 92, 061106 (2008).
- [48] G. Genoud, F. Wojda, M. Burza, A. Persson, and C.-G. Wahlström, Active control of the pointing of a multi-terawatt laser, Rev. Sci. Instrum. 82, 033102 (2011).
- [49] K. Tyszka and M. Dobosz, Laser beam angular stabilization system based on a compact interferometer and a precise doublewedge deflector, Rev. Sci. Instrum. 89, 085121 (2018).
- [50] C. Ding, D. Zhu, Z. Wei, M. Tang, C. Kuang, and X. Liu, A compact and high-precision method for active beam stabilization system, Opt. Commun. 500, 127328 (2021).
- [51] M. Litos, E. Adli, W. An, C. I. Clarke, C. E. Clayton, S. Corde, J. P. Delahaye, R. J. England, A. S. Fisher, J. Frederico *et al.*, High-efficiency acceleration of an electron beam in a plasma wakefield accelerator, Nature (London) 515, 92 (2014).
- [52] D. E. Manolopoulos, Derivation and reflection properties of a transmission-free absorbing potential, J. Chem. Phys. 117, 9552 (2002).
- [53] M. V. Ammosov, N. B. Delone, and V. P. Krainov, Tunnel ionization of complex atoms and of atomic ions in an alternating electromagnetic field, Sov. Phys. JETP **64**, 1191 (1986).
- [54] P. Sprangle, E. Esarey, and A. Ting, Nonlinear Theory of Intense Laser-Plasma Interactions, Phys. Rev. Lett. 64, 2011 (1990).